Assessing Calibration Stability Using the Global Precipitation Measurement (GPM) Microwave Imager (GMI) Noise Diodes

David W. Draper, *Member, IEEE*, David A. Newell, Darren S. McKague, *Member, IEEE*, and Jeffrey R. Piepmeier, *Senior Member, IEEE*

***Abstract*—With rising demand for smaller, lower mass microwave instruments, internal calibration using noise diodes is becoming increasingly more attractive for space-borne radiometer applications. Since noise diodes can exhibit on-orbit excess temperature drift, internally calibrated systems typically require vicarious on-orbit recharacterization. The GMI is the first instrument of its kind to include both internal (noise diodes) and external (hot load/cold sky) calibration systems. The dual-calibration system provides the unprecedented capability to directly measure transient behaviors in the hot load, cold sky view, and receiver nonlinearity. Furthermore, the behavior of the noise diodes can be directly evaluated, which may shed light on improvements to internal calibration for future missions. This paper directly examines the behavior of the GMI noise diodes using the hot load and cold sky views for the first 6 months of operations. Two of the seven channels with noise diodes have exhibited on-orbit noise diode excess temperature drift of about 1 K. The other noise diodes have remained exceptionally stable. The noise diodes are used to evaluate transient behaviors in the GMI hot load, cold sky view, and nonlinearity. The hot-load brightness temperature variation due to gradients is re-evaluated and shown to be smaller at the lower frequencies than at preflight calibration. Radio frequency interference (RFI) in the cold view is evaluated using the noise diode backup calibration. The on-orbit nonlinearity is trended over the first 6 months and shown to be stable over that time period.**

***Index Terms*—Calibration, microwave radiometry, noise diodes.**

I. Introduction

THE Global Precipitation Measurement (GPM) core observatory was launched on February 27, 2014 at 18:37 UT from Tanegashema, Japan, carrying two science instruments, the dual-frequency precipitation radar (DPR), and the GPM Microwave Imager (GMI). The GMI is a conical scanning radiometer with the primary mission to measure precipitation from space [1]. The GMI instrument was built by Ball Aerospace under contract from NASA's Goddard Space Flight Center. The GPM mission consists of a constellation of international partner microwave sensors [2]. The GPM core observatory operates in a 65° inclination orbit and is intended to be the cross-calibration standard for radiometer precipitation measurements made by other GPM constellation members. The GMI consists of 13 radiometric channels at the following frequencies and polarizations: 10.65 GHz (v/h), 18.7 GHz (v/h), 23.8 GHz (v), 36.64 GHz (v/h), 89 GHz (v/h), 166 GHz (v/h), and 183.31 ($\pm 3, \pm 7$) GHz (v) [2] where "v" indicates a vertical polarization channel and "h" indicates a horizontal polarization channel. The GMI uses an on-board calibration system to provide a means to convert from raw digital measurements to antenna temperature (T_a). The primary on-board calibration system consists of a conventional hot load (RF blackbody) and cold sky reflector which are viewed by the feed horns on each scan. The instrument also uses internal noise diodes on the low-frequency channels (10.65–36.64 GHz) that couple RF energy into the RF chain during the hot and cold views on every other scan to provide two additional calibration points (cold + noise and hot + noise). The noise diodes along with the conventional hot and cold views provide a dual-calibration system for the seven lowest frequency channels [3]. The locations of the GMI noise diode assemblies within the GMI instrument electronics bay are shown in Fig. 1. A notional diagram showing the four calibration points is given in Fig. 2.

GMI calibration system stability is critical to providing a consistent standard by which other radiometers may be cross-calibrated. The dual-calibration system on GMI is a key element to assessing and improving calibration stability in both ground and on-orbit calibration. Assuming the noise diode excess temperature is well known, the noise diodes provide a "backup" method to measure the gain of the receiver. During ground and early on-orbit calibration, the noise diode excess temperature is characterized as a function of physical temperature by directly measuring it with the primary calibration sources over temperature. Once the noise diode excess temperature is characterized as a function of physical temperature, the gain determined by the characterized noise diodes should closely match that are measured by the hot and cold views. The noise diodes can then be used stand-alone to measure the receiver gain. Using the noise diodes to measure gain provides a stability check of the hot load and cold views. Transient calibration anomalies, drifts, or cyclical variations in the hot or

Manuscript received August 29, 2014; revised December 09, 2014; accepted February 13, 2015. Date of publication March 17, 2015; date of current version December 21, 2015. This work was supported by the Goddard Space Flight Center GPM program.

D. W. Draper and D. A. Newell are with the Ball Aerospace & Technologies Corporation, Boulder, CO 80301 USA (e-mail: ddraper@ball.com; dnewell@ball.com).

D. S. McKague is with the Department of Atmospheric, Oceanic, and Space Sciences, University of Michigan, Ann Arbor, MI 48109 USA (e-mail: dmckague@umich.edu).

J. R. Piepmeier is with the NASA Goddard Space Flight Center, Greenbelt, MD 20771 USA (e-mail: jeffrey.r.piepmeier@nasa.gov).

Color versions of one or more of the figures in this paper are available online at http://ieeexplore.ieee.org.

Digital Object Identifier 10.1109/JSTARS.2015.2406661

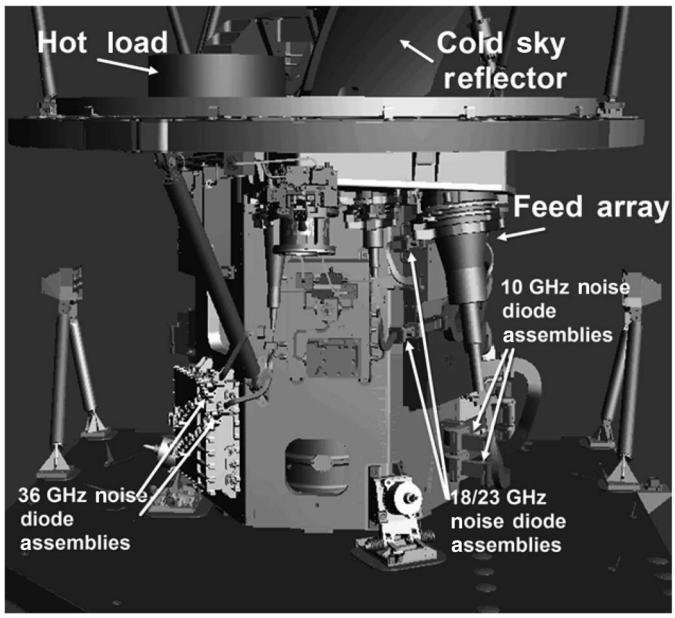

Fig. 1. GMI electronics bay showing the locations of the various noise diode assemblies, feed array, hot load, and cold sky reflector. The GMI reflector (not shown) attaches to the struts extending upward above the electronics bay. The reflector and electronics bay rotate while the hot load and cold sky reflector remain stationary.

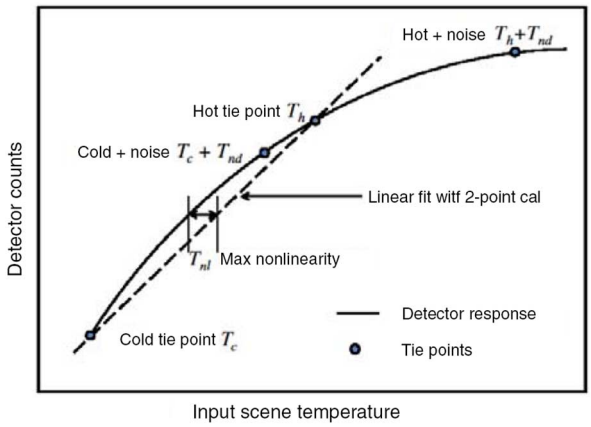

Fig. 2. Notional diagram showing the four GMI calibration points, the ideal linear response (dashed), and nonlinear system response (black, highly exaggerated).

cold views can be detected by comparing the conventional hot brightness temperature to that measured by the instrument using the other calibration source with the noise diodes. This methodology does not provide an absolute calibration assessment, but an assessment of changes that have occurred in the calibration sources from the time the noise diodes are characterized.

In addition to the dual-calibration system, several unique features aid to increase GMI's calibration accuracy and stability. The GMI uses very tight shrouding around the hot load to keep the sun from heating the surface of the hot load. The GMI cold sky reflector is oversized to limit spillover, and the GMI cold sky and main reflectors use a proven coating to provide a very high reflectivity that reduces self-emissions from the antenna [4].

Because the GMI instrument has both internal and conventional external calibration, it provides an excellent case study for evaluating the reliability of internal calibration systems for radiometric instruments. Internal calibration provides significant mass and complexity savings over conventional calibration methods, but can often require extensive on-orbit calibration [5], [6]. The GMI calibration measurements afford a near-constant evaluation of the noise diode excess temperature stability.

This paper focuses on three main topics: the use of the noise diodes in the ground calibration, the ground and on-orbit calibration stability of the noise diodes, and the use of the noise diodes to determine the on-orbit stability of the primary calibration system. In assessing the primary calibration system, we particularly examine the hot-load gradient correction, radio frequency interference (RFI) in the cold sky view, and characterization of the receiver nonlinearity. With the dual-calibration system, anomalous transient behavior in the hot load or cold sky views is quickly identified without the use of vicarious calibration methods.

II. Calibration Equations

During each 1.875-s conical scan of the GMI antenna, the GMI measures three sectors: the earth view (approximately 152° of the scan, centered on the spacecraft ground track), the hot load view, and the cold sky view. The noise diodes operate during the calibration view for every other scan providing four calibration points: 1) cold, 2) $\mathrm{cold} + \mathrm{noise}$, 3) hot, and 4) $\mathrm{hot} + \mathrm{noise}$. The baseline GMI calibration scheme uses the hot load and cold sky view along with precharacterized nonlinearity to relate observed counts to antenna temperature. Calibration is performed using the radiometric transfer function (RTF) [7]

$$T_a = T_c + \frac{C_s - C_c}{g} + u\frac{(C_s - C_c)(C_s - C_h)}{g^2} \tag{1}$$

$$g = (C_h - C_c)/(T_h - T_c) \tag{2}$$

$$u = 4T_{nl}/(T_h - T_c)^2 \tag{3}$$

where T_c and T_h are the cold and hot view brightness temperatures, C_s, C_h, and C_c are the scene counts, hot counts, and cold counts, respectively, g is the gain calculated between the two calibration views, u is the normalized nonlinearity that has been characterized beforehand [8], and T_{nl} is the maximum nonlinearity in Kelvin between the hot and cold calibration views.

In nominal conditions, the four calibration points allow determination of four parameters: the gain (g), offset ($T_c - C_c/g$), excess temperature of the noise diodes T_{nd}, and the nonlinearity T_{nl}. The first two parameters are solved with the cold and hot views alone. Solving the RTF for the two noise diode views ($\mathrm{cold} + \mathrm{noise}$ and $\mathrm{hot} + \mathrm{noise}$), the noise diode excess temperature can be directly computed using the following equation:

$$T_{nd} = [T_h - T_c]\,\frac{x_{cn}(x_{hn} - x_{hn}^2) - (x_{hn} - 1)(x_{cn} - x_{cn}^2)}{x_{hn} - x_{cn} + x_{cn}^2 - x_{hn}^2} \tag{4}$$

where $x_{cn} = (C_{cn} - C_c)/(C_h - C_c)$, $x_{hn} = (C_{hn} - C_c)/(C_h - C_c)$, and C_{cn} and C_{hn} are the cold + noise and hot + noise counts.

Likewise, the nonlinearity can be directly computed using the following equation:

$$T_{nl} = [T_h - T_c] \frac{x_{hn} - x_{cn} - 1}{4(x_{hn} - x_{cn} + x_{cn}^2 - x_{hn}^2)}. \quad (5)$$

The noise diode excess temperature and nonlinearity are trended as a function of physical temperature and regressed as a quadratic

$$T_{nd-trended} = a_0 + a_1 T_{phys-nd} + a_2 T_{phys-nd}^2 \quad (6)$$

$$T_{nl-trended} = b_0 + b_1 T_{phys-rcvr} + b_2 T_{phys-rcvr}^2 \quad (7)$$

where $T_{phys-nd}$ is the physical temperature of the noise diode assembly and $T_{phys-rcvr}$ is the physical temperature of the receiver. The trended noise diode excess temperature and nonlinearity depend only on the physical temperature of the receiver, and are thus not subject to transient errors in the hot and cold views, providing an excellent method to detect such errors.

Once the noise diodes have been adequately characterized as function of the noise diode physical temperature, the cold and cold + noise views can be used as a backup method to calibrate the instrument

$$T_{a1} = T_c + \frac{C_s - C_c}{g_1} + u\frac{(C_s - C_c)(C_s - C_{cn})}{g_1^2} \quad (8)$$

where $g_1 = (C_{cn} - C_c)/T_{nd-trended}$. Likewise, the hot and hot + noise views can be used to calibrate the instrument

$$T_{a2} = T_h + \frac{C_s - C_h}{g_2} + u\frac{(C_s - C_h)(C_s - C_{hn})}{g_2^2} \quad (9)$$

where $\mathrm{g_2} = (\mathrm{C_{hn}} - \mathrm{C_h})/\mathrm{T}_{nd-trended}$.

The backup calibration affords a method to check the stability of the primary calibration sources. The hot and cold view brightness temperatures can be calculated using the backup calibration by replacing C_s in (8) with C_h and replacing C_s in (9) with C_c

$$T_{h-backup} = T_c + \frac{C_h - C_c}{g_1} + u\frac{(C_h - C_c)(C_h - C_{cn})}{g_1^2} \quad (10)$$

$$T_{c-backup} = T_h + \frac{C_c - C_h}{g_2} + u\frac{(C_c - C_h)(C_c - C_{hn})}{g_2^2}. \quad (11)$$

Because the hot load and cold sky views are initially used to trend the noise diode excess temperature over physical temperature, $T_{h-backup}$ and $T_{c-backup}$ should match T_h and T_c to within the radiometric sensitivity of the receivers and the accuracy of the noise diode trend parameterization. Additional deviations in hot and cold view temperatures from the temperature inferred from (10) and (11) that occur after the noise diode trend is established can only be attributed to a calibration error in one or more of the calibration elements. If calibration errors occur in multiple elements, the errors must have sufficiently different characteristics that they can be separated one from another in order to properly understand and mitigate the error. Once an error has been identified, it is usually obvious from the data of which element (hot load, cold sky view, noise diode, or receiver) is at fault based on the nature of the error. The errors may be transient in nature (persist for a finite amount of time), may be cyclical (exhibit a pattern from orbit to orbit), or may represent a long-term drift of the element. The result of (10) or (11) can be used to evaluate the nature of the error and mitigate it by properly modifying the ground algorithms.

III. GMI Ground Calibration Test Results

This section illustrates the utility of the noise diodes to improve the accuracy of the ground calibration. The GMI ground calibration test was performed as part of the GMI thermal vacuum test program during December 2011. During the calibration test, the GMI instrument viewed two external blackbody targets: a cold target cooled with liquid nitrogen to about 100 K and a variable target that transitioned in temperature between 100 and 340 K. The cold target replaced the cold sky view, and the variable target was used to simulate the earth-scene view. The two targets were positioned in direct line-of-sight of the feed horns and provided a method of evaluating instrument radiometric accuracy relative to an external calibration system. During the thermal vacuum test, the GMI noise diodes were cycled ON and OFF every two scans, affording trending of the noise diode excess temperature over the physical temperature of the noise diodes using (4). The noise diodes excess temperature was fit with a second-order polynomial to allow determination of the noise diode excess temperature at an arbitrary noise diode physical temperature using (6).

A difficulty with ground calibration test using cryogenically cooled targets is maintaining solid, spatially even, thermal conduction between the target-absorbing surface and the cooling plate since the target surface is exposed to warming from the surrounding environment. Ball performed extensive modeling and validation on the calibration targets to understand and correct the gradients between the target surface and the platinum resistance thermometers (PRTs). A gradient correction was applied to the data based on the assumption of perfect conduction between different layers in the calibration system [4]. For the GMI calibration, it was apparent that the models did not fully capture the thermal conduction imperfections, leading to additional errors in the estimated cold target brightness temperature. As the variable target increased in temperature, it warmed the top deck of the instrument, which then coupled heat into the cold target. The cold target temperature and the associated T_c error increased as the cold target was heated by the top deck.

The residual error associated with the cold target can be identified using the hot and hot + noise measurements, since it varies with the variable target temperature over the duration of the test. Fig. 3 shows the variable target temperature, the cold target temperature T_c, and the cold target temperature measured by the GMI using the hot and hot + noise views to perform backup calibration $T_{c-backup}$. The difference between

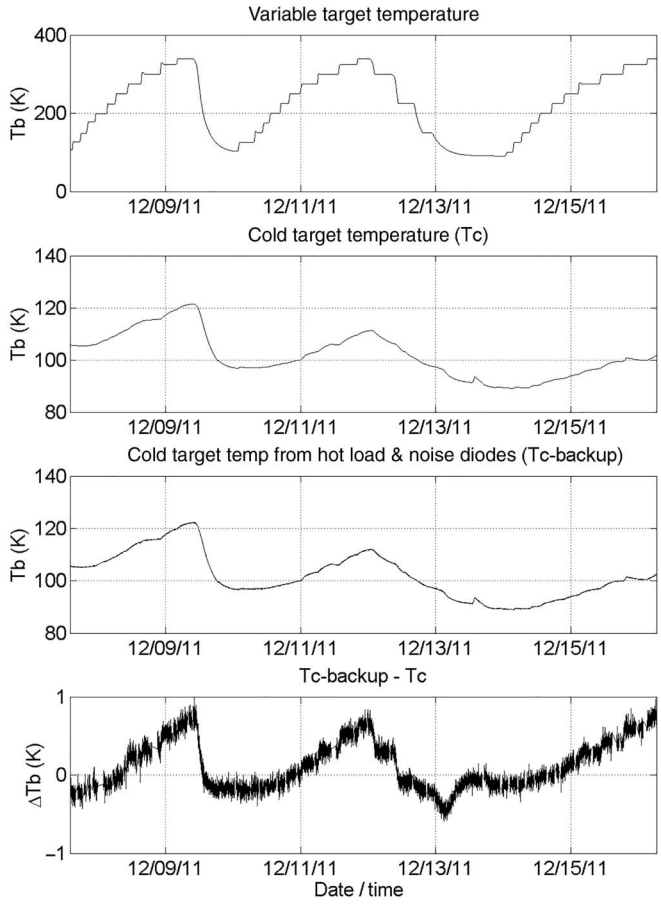

Fig. 3. Top: Variable target temperature over the duration of the GMI calibration test. Second from top: Cold target-measured brightness temperature using PRTs in the target. Third from top: GMI-measured cold target brightness temperature (36 GHz) using the hot load and noise diodes as calibration references. Bottom: Difference between cold target temperature and the GMI-measured cold target brightness temperature.

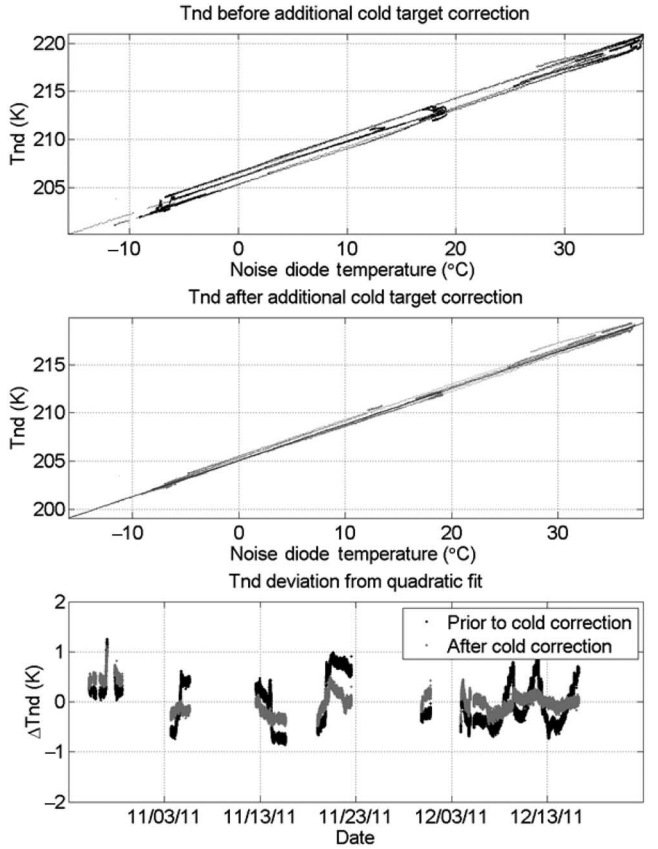

Fig. 4. Top: 36 GHz H-pol noise diode excess temperature as a function of noise diode temperature. Middle: 36 GHz H-pol noise diode excess temperature after the additional cold target correction. Bottom: 36 GHz H-pol noise diode excess temperature deviation from quadratic fit as a function of time. The black is before the additional cold target correction and the gray is after the additional cold target correction.

the T_c and $T_{c-backup}$ is shown in the bottom plot of Fig. 3. This figure demonstrates that a residual error exists in the cold target brightness temperature that is not fully captured in the blackbody gradient correction. The cold target error increases with variable target temperature as more radiant energy is coupled from the variable target to the cold target via the top deck, exacerbating the gradient-induced errors in T_c.

Because the noise diode excess temperature is computed using T_c from (4), the computed value of T_{nd} is also directly influenced by error in T_c. Therefore, an error in T_c translates directly into an error in computed T_{nd}. Because of the relationship, the noise diode excess temperature error to the model fit could be used to troubleshoot the cold target. The T_c gradient correction was adjusted by iteratively scaling the cold target gradient correction, recomputing T_{nd} from (4), and regressing the $T_{nd-trended}$ quadratic fit over temperature until the error between the measured noise diode excess temperature and the quadratic fit was minimized. This method did not remove constant or absolute biases in the cold target temperature, only temperature-dependent biases. Some of the channels required a factor of 3 adjustment in the cold gradient correction, which changed the cold blackbody brightness temperature by 1–2 K. The corrected T_{nd} is shown in Fig. 4. This exercise demonstrates the utility of the noise diodes in correcting temperature-varying errors in the calibration targets used during ground testing. Along with the use of the noise diodes to improve the ground calibration, the ground calibration cold target thermal conduction and isolation have been dramatically improved since the core GMI test for use in future calibrations to provide more accurate and stable references.

IV. Preflight Noise Diode Stability

In order to use the noise diodes as a backup calibration source on-orbit, it is required that the noise diode excess temperature be sufficiently stable so as to adequately predict the noise diode excess temperature over significant portions of an orbit. The ground calibration can be used to assess the stability of the noise diodes by demonstrating how well a second-order polynomial can be used to predict the noise diode excess temperature over the duration of the thermal vacuum test.

Fig. 4 shows the 36-GHz H-pol noise diode excess temperature as a function of noise diode physical temperature prior to and after correcting for the cold target gradients identified in Section III. For this particular noise diode, the quadratic fit can adequately represent the noise diode temperature to within

TABLE I
ERROR BETWEEN TND AND TND_TRENDED FOR GROUND TEST AND ON-ORBIT OPERATIONS FOR THE FIRST 6 MONTHS OF GMI OPERATIONS

Channel	Ground test $3\times$ rms error (with cold target correction) (K)	On-orbit drift in the first 24 days* (K)	On-orbit $3\times$ rms error after the first 24 days (K)
10.65 GHz V	2.6	0.8	0.4
10.65 GHz H	1.0	0.1	0.22
18.7 GHz V	0.4	0.2	0.23
18.7 GHz H	0.4	0.1	0.25
23.8 GHz V	0.4	0.2	0.17
36.64 GHz V	0.8	0.8	0.39
36.64 GHz H	0.7	0.15	0.20

*The noise diode characterization changed from ground to on-orbit (see Fig. 5) likely due to calibration differences between the ground cold target and on-orbit cold sky view. The "on-orbit drift" column does not reflect that change. It only reflects the drift exhibited from day 1 on-orbit.

about 0.7 K over the nearly 2-month duration of the GMI thermal vacuum testing. The rms error of all noise diode excess temperatures relative the quadratic fits (multiplied by 3, to yield an approximate 3-sigma variation) is given in Table I. In general, the physical temperature of the noise diodes can be used to predict the excess temperature to within 1 K for all noise diodes except 10.65 GHz V-pol, which exhibited significant drift over the duration of the ground test. We note that because the noise diodes were used to correct errors in the cold target temperature, it is possible that a portion the noise diode excess temperature drift was transferred to the ground T_c. However, the true change in T_{nd} is a slow non-thermal-dependent drift, while the apparent change in T_{nd} due to T_c error is directly correlated to the temperature differential between the top deck and cold target. The two effects are therefore highly independent and can be separated with confidence.

V. ON-ORBIT NOISE DIODE STABILITY

In this section, we examine the on-orbit stability of the noise diodes. For data taken during the first 5 months on-orbit with the flight cold sky reflector, the noise diode excess temperature characterization was rebaselined to remove any further biases caused by the ground system or initial on-orbit drift. The rebaselining utilized (4) to compute the noise diode excess temperature and determined an updated parameterization (6) by adjusting the ground-determined quadratic fit to physical temperature to match the on-orbit excess temperature. The reparameterization ignored all data prior to March 24th, all known RFI events in the cold view, and all 4-sigma outliers. The rebaselining removed an additional bias in the noise diode excess temperature characterization relative to the ground measurements. The rebaselined fit is compared to the original ground fit in Fig. 5.

The on-orbit derived noise diode excess temperature is compared to the rebaselined quadratic over the 6 months of operation in Fig. 6. There was some settling of the noise diodes during the first 24 days. We compute two stability metrics of the noise diodes: the mean drift over the first 24 days and the on-orbit variation after the first 24 days. The mean drift is

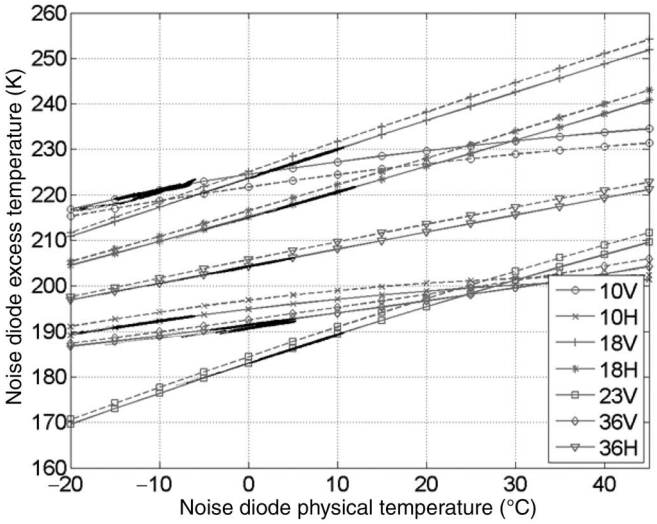

Fig. 5. Noise diode excess temperature characterization for each GMI channel with noise diodes. The dashed lines represent the ground characterization and the solid lines represent the on-orbit recharacterization. The black dots are the on-orbit derived excess temperature [9].

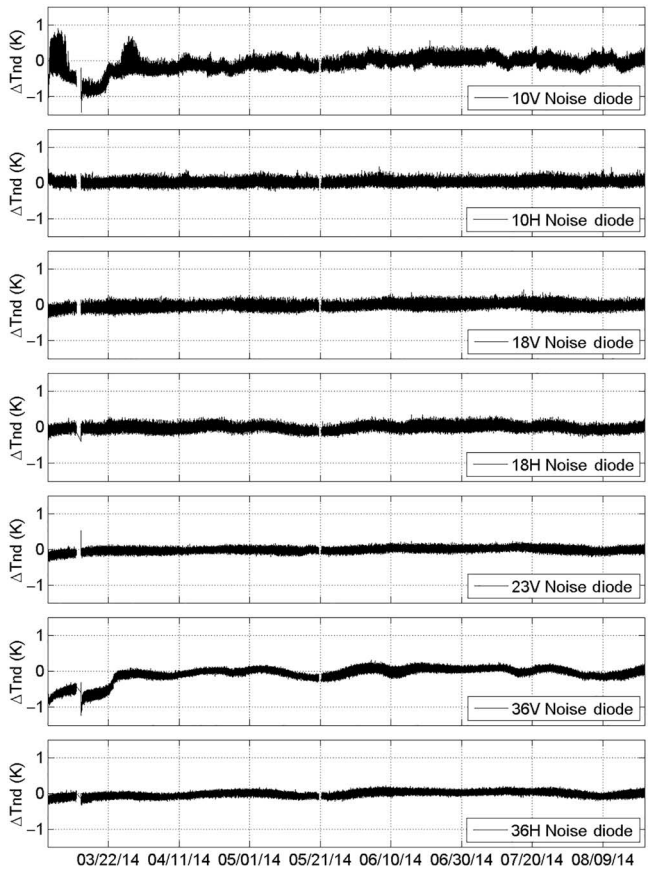

Fig. 6. Noise diode excess temperature deviation from the on-orbit recharacterized model fit as a function of time.

defined as the deviation of the noise diode excess temperature from the quadratic fit, averaged over an orbit. The on-orbit variation is defined as 3 times the rms noise diode error between the measured and trended excess temperatures. The mean drift and on-orbit variation are tabulated in Table I. The metrics indicate

the predictability of the noise diode excess temperature using the simple quadratic fit. Five of the seven channels demonstrate a noise-diode predictability of 0.3 K. Based on the errors shown in Table I, it is clear that the 10.65-V-pol noise diode and the 36.64-V-pol noise diode experienced early on-orbit drift of about 0.8 K and are generally slightly more variable than the other noise diodes. There is a shift in noise diode excess temperature behavior around 3/22/2014 for both 36.64 and 10.65 V noise diodes. The GMI noise diodes will continue to be monitored for stability. As with other microwave instruments with noise diodes such as Aquarius [10], it appears that the GMI noise diodes that exhibited early on-orbit drift have largely stabilized with continued on-orbit operation. The exception is the 10.65-v-pol noise diode which has continued drift and exhibit larger variations on-orbit.

The on-orbit performance of the GMI noise diodes provides three major observations about the noise diode assemblies. First, drift in the excess temperature can vary significantly between seemingly identical parts as illustrated by the comparison between the 10.65-v-pol and 10.65-h-pol noise diodes. Second, the noise diodes that exhibit initial drift also have generally larger noise diode excess temperature variability over time. Third, drift may be detected in ground measurements. These observations suggest that noise diode on-orbit drift may be mitigated on future sensors by prescreening noise diode assemblies, and selecting to use those serial numbers that exhibit limited or no drift in ground measurements over several weeks of operations under vacuum. Such screening would be especially useful for missions that employ only internal calibration.

VI. GMI Hot Load Stability

The noise diode backup calibration is used in this section to assess and improve the calibration of the hot load by providing more precise characterization of the thermal-induced biases. The GMI hot load consists of a periodic array of metal pyramids coated with an RF-absorbent material [4]. On each scan, the GMI feed horns view the hot load. The GMI hot load temperature is measured using PRTs embedded in the metal portion of the pyramids. The GMI hot load brightness temperature calibration assumes the target has nearly unity emissivity, the beam fraction of the feedhorn on the hot load is very high, and any standing waves between the target and the feed are negligible. When gradients exist in the target from tip to base, the hot load PRT measurements $\bar{T}_{h-prt}$ do not always reflect the RF-viewed aggregate brightness temperature T_h. The calibration algorithm computes the brightness temperature viewed by the feeds as the PRT-measured temperature of the target plus a vertical gradient term $\Delta\bar{T}_{RF-base}$ that represents the average brightness temperature difference between the absorber as viewed in the RF and the metal portion containing the PRTs [4]

$$T_h = \bar{T}_{h-prt} + \Delta\bar{T}_{RF-base} \tag{12}$$

where $\bar{T}_{h-prt}$ is the average temperature of the PRTs over the hot load track viewed by the feeds.

For GMI, the vertical gradient term $\Delta\bar{T}_{RF-base}$ is driven primarily by radiative coupling between the hot load tray (directly facing the hot load) and the hot load itself. For the operational algorithm, $\Delta\bar{T}_{RF-base}$ has been parameterized using the difference between the hot load tray temperature and the hot load PRT measurement [4]

$$\Delta\bar{T}_{RF-base} \cong \sum_{k=0}^{3} u_k \left(T_{hl-tray} - \bar{T}_{h-prt}\right)^k \tag{13}$$

where u_k are empirically derived cubic coefficients. The original u_k were derived based on multiple ground analyses and tests as described in [4].

The hot load tray temperature can vary significantly for each orbit, while the hot load temperature is relatively stable. Since the hot load tray temperature varies in a cyclical manner for each orbit, hot load vertical gradient term $\Delta\bar{T}_{RF-base}$ is cyclical as well. The transient behavior of the gradient provides an excellent opportunity to use the cold + noise diode backup calibration (which should not exhibit the cyclical pattern) to identify possible errors in the preflight hot load gradient correction and adjust the gradient correction accordingly.

Assuming no other error sources, the $\Delta\bar{T}_{RF-base}$ term is determined by the difference between the backup hot load temperature and the hot load PRT measurement $(T_{h-backup} - \bar{T}_{h-prt})$. The $(T_{h-backup} - \bar{T}_{h-prt})$ are shown in Fig. 7 versus $(T_{hl-tray} - \bar{T}_{h-prt})$. To determine better fit coefficients for (13), the hot load gradient correction $\Delta\bar{T}_{RF-base}$ determined in preflight calibration [4] is scaled for each channel to minimize the error in the noise diode excess temperature; similar to what was done for the ground cold target analysis in Section III. Because the ground analysis contended with the additional gradient errors in the cold blackbody, there was still some uncertainty in the hot load gradient correction which caused us to conservatively assume all channels exhibited about the same gradient variation. An interesting discovery from the on-orbit study is that there is a significant frequency dependence on the hot load gradient error. Fig. 7 shows a steady increase in the magnitude of the on-orbit adjusted hot load gradient correction as a function of frequency from around 0.2 K min to max at 10 GHz to around 0.5 K min to max at 37 GHz.

VII. RFI in the GMI Cold View

The GMI backup calibration method also provides a method to quickly identify transient errors in the cold sky view. Two types of errors have been identified: moon intrusion and RFI from geosynchronous satellites directly entering the cold sky beam. The moon regularly enters the cold sky field of view and is removed in the operational algorithm using a geometric filter. This section focuses on the cold view RFI, provides an assessment of the cold view RFI using the noise diodes, and demonstrates how the noise diodes were used to train a count-level detection algorithm to mitigate the RFI.

The National Telecommunications and Information Administration (NTIA) provides the allocations for use of the RF spectrum within and around the GMI frequency

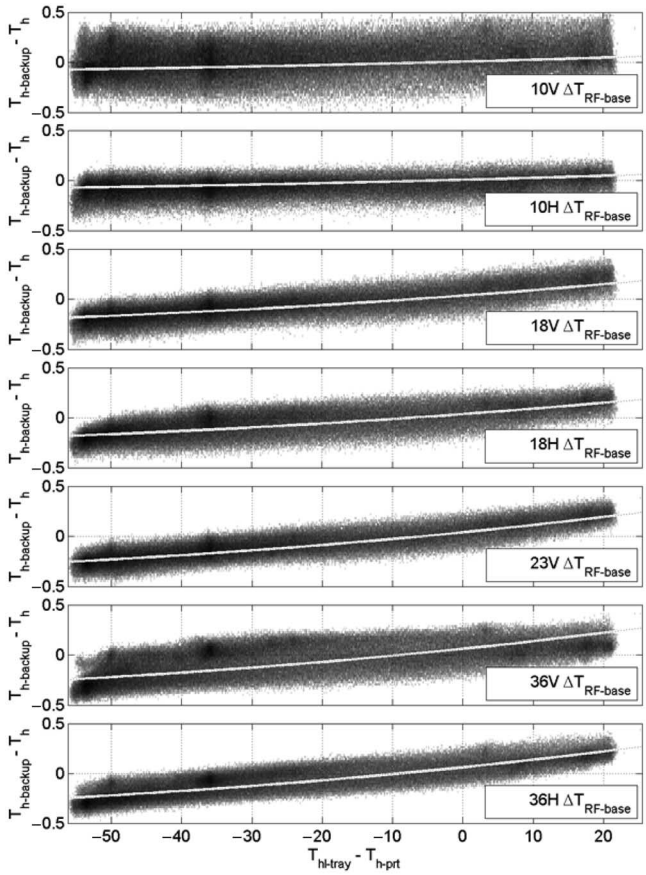

Fig. 7. GMI hot load gradient correction for each channel with noise diodes. Each plot shows a 2-D histogram of the difference between the backup hot load temperature and the PRT measurements. It also shows the on-orbit adjusted hot load gradient correction for each channel (white lines) [9].

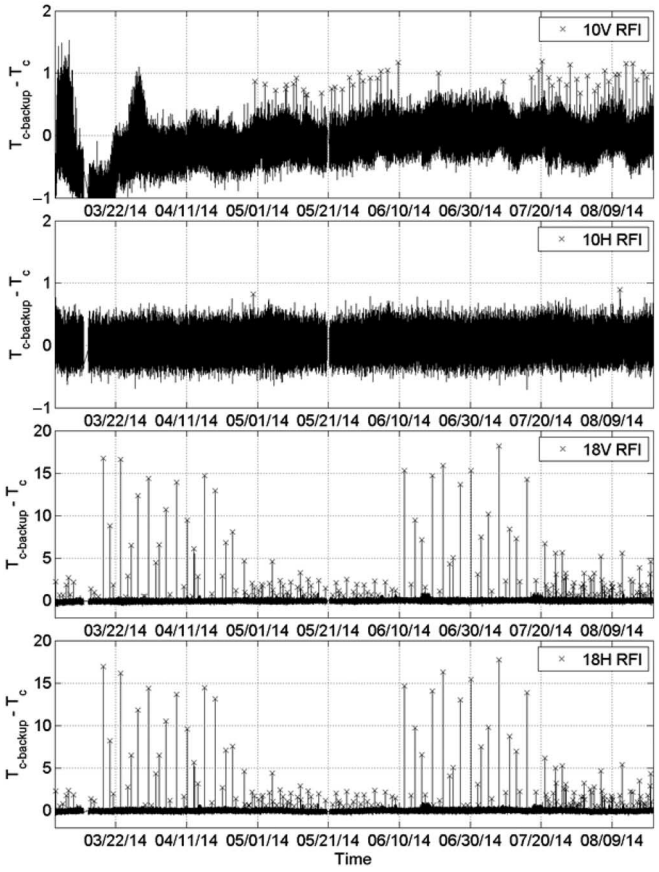

Fig. 8. Backup calibration for the cold view compared to the ideal cold view temperature as a function of time for the 10.65- and 18.7-GHz channels. RFI events are displayed with "x's."

bands. The GMI utilizes bands that are allocated for passive earth exploration and shared with other ostensibly noninterfering applications. Some direct broadcasting satellites utilize C- and Ku-band transmitters and are permitted per NTIA allocations to downlink (but not up-link) within the 18.7-GHz GMI band. For example, the DirecTV-10, -11, and -12 satellites utilize the 18.3–18.8 GHz frequency block for one-way broadcast HDTV [11]. Geosynchronous satellites are also permitted to transmit adjacent to the 10.65-GHz band starting at 10.7 GHz [12]. Such transmissions in or near the GMI bands interfere with the cold sky view as the cold sky beam passes through their line-of-sight.

We examine the magnitude of RFI events in the GMI cold sky view. This is done by comparing the backup cold view temperature from the hot and hot + noise views to the apparent brightness temperature of cold space defined as 2.73 K with appropriate adjustments for the Rayleigh–Jeans approximation to Planck's law [7]. The results of the comparison are shown in Fig. 8. RFI is evidenced by the spikes in the data. We have identified data as having RFI contamination when the backup cold view brightness temperature exceeds the ideal temperature plus the mean drift by 0.75 K for the 10.65-GHz channels and 0.55 K for the 18.7-GHz channels (definition of mean drift is given in Section VI). The 18.7- and 10.65-GHz frequencies exhibit RFI in the cold view. No cold view RFI has been noted in any other GMI channels. Low-level RFI on the order of 1 K is flagged on the 10.65-GHz v-pol channel mainly during conditions where the spacecraft is flying in the 0° yaw orientation. The 10.65-GHz h-pol channel does not exhibit any significant RFI. The 18-GHz channels both show relatively high-level RFI. While the spacecraft is traveling in the 180° yaw orientation, the 18.7-GHz RFI can affect the multiscan average cold counts by up to 20 K. In the 0° yaw orientation, the RFI effect on multiscan-averaged cold counts is typically less than 5 K. Over 150 cold view RFI events occurred on the GMI 18.7-GHz channels during the first 6 months.

The RFI flagged by the noise diodes has been used to formulate an RFI database to train a cold sky RFI filtering algorithm to be used in the operational calibration algorithm. The RFI filter identifies and flags RFI in the cold swath by looking for abnormal measurements in the cold swath versus the scan average (averaged over multiple scans), removing the abnormally high measurements, robustly dilating, and iterating the process several times to remove the RFI from the cold swath. The robust dilation identifies and flags an $M \times N$ region as being corrupt if multiple cells within the region are above a threshold relative to the scan average or have been flagged on a previous iteration. Otherwise, the flagging is removed. Requiring multiple neighboring cells to be above the threshold relative to the scan average allows the thresholds to be set to about 130% of the NEDT and still not produce significant false alarms. The

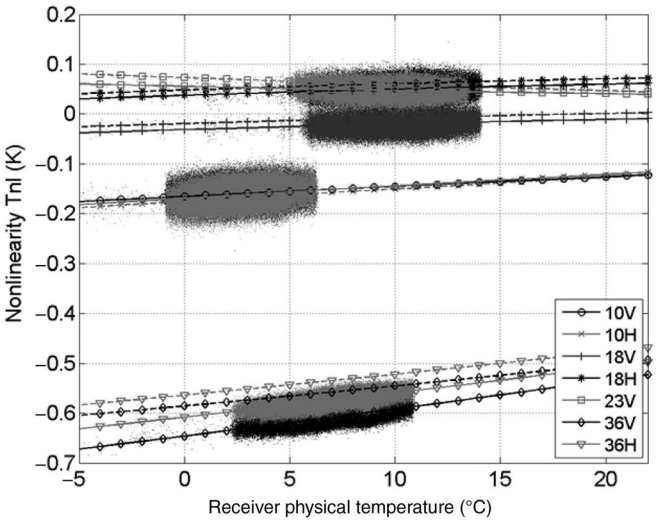

Fig. 9. Nonlinearity characterization for each GMI channel with noise diodes. The dashed lines represent the ground characterization, and the solid lines represent the on-orbit recharacterization. The dots represent the on-orbit derived nonlinearity [9]. Note that the nonlinearity value shown here has been normalized to hot and cold tie points of 300 and 3 K.

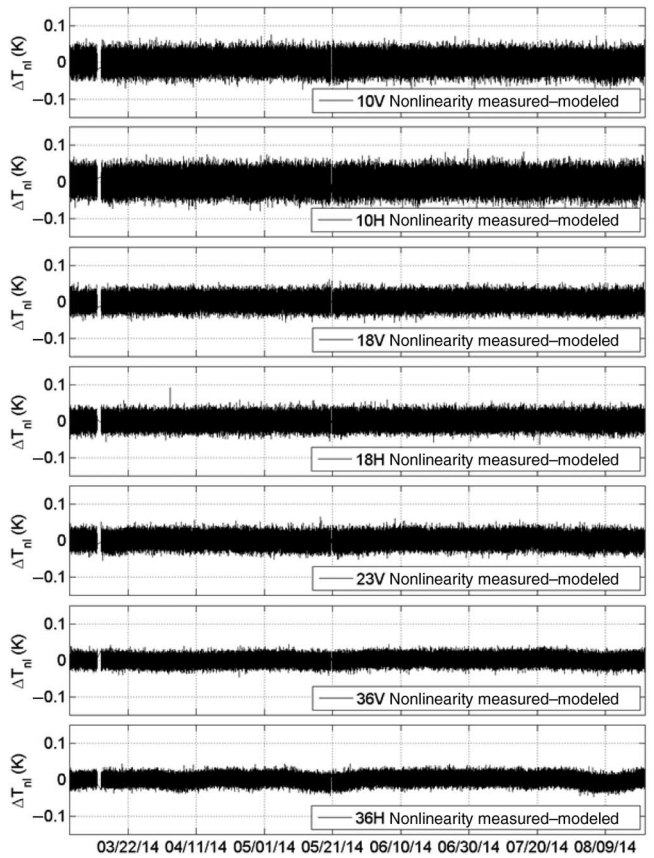

Fig. 10. Nonlinearity deviation from the model fit as a function of time.

algorithm removes the corrupted measurements from the scan average for subsequent iterations. The filtering method is preferred in the flight algorithm instead of noise diode detection because it can be performed on the cold swath alone prior to any further processing. The dual-calibration flagging method from this section was key to identifying low-level RFI for training the flight algorithm that was not otherwise easily detectible, thus improving the quality of the RFI flagging algorithm.

VIII. GMI Nonlinearity Stability

In this section, we examine the stability of the nonlinearity over the first 6 months. Nonlinearity is typically measured during ground calibration, but is difficult to evaluate on orbit with two-point calibration schemes. The GMI noise diodes provide the method to constantly measure nonlinearity on-orbit using the method given in Section II in order to understand its stability. The quadratic nonlinearity characterization versus receiver temperature was updated on-orbit for the channels with noise diodes based on the on-orbit measurements. The ground and on-orbit nonlinearity measurements only differ by a few hundredths of a Kelvin as shown in Fig. 9.

The difference between ground and on-orbit characterization is shown in Fig. 10 as a function of time. There has been no appreciable drift in the nonlinearity characterization during that time. The nonlinearity will continue to be analyzed in order to evaluate if the receiver nonlinearity changes over time.

IX. Conclusion

The noise diodes on GMI serve as a diagnostic tool to identify transient anomalous behavior of the GMI primary calibration system. This paper has demonstrated how the noise diodes have been used to improve the hot load calibration and identify RFI in the cold view. The noise diodes also afford nonlinearity trending on the low frequency channels over the life of the instrument. Excluding the first 24 days, on-orbit data show that the excess temperature of the noise diodes are predictable to within about 0.2–0.4K over the first 6 months of operations. The 36-GHz v-pol noise diode has exhibited noticeable early drift, but has largely stabilized. The 10-GHz v-pol noise diode has continued to drift and vary more than the other noise diodes. Stability of the GMI noise diodes will continue to be monitored throughout the life of the instrument.

For instruments with internal calibration, the GMI experience suggests that noise diode assemblies should be prescreened for drift prior to selection for flight. Noise diode assemblies that experience drift in performance under vacuum over a period of several weeks will likely experience drift and higher temporal variability on orbit.

References

[1] Y. Hou *et al.*, "The global precipitation measurement mission," *Bull. Amer. Meteorol. Soc.*, vol. 95, pp. 701–722, 2013.

[2] D. W. Draper *et al.*, "The global precipitation measurement (GPM) microwave imager (GMI): Instrument overview and early on-orbit performance," *IEEE J. Sel. Topics Geosci. Remote Sens.*, 2015, to be published.

[3] J. B. Sechler, "GPM microwave imager selected calibration features and predicted performance," in *Proc. IEEE Int. Geosci. Remote Sens. Symp. (IGARSS)*, 2007, pp. 5237–5239.

[4] D. W. Draper, D. A. Newell, D. A. Teusch, and P.K. Yoho, "Global precipitation measurement microwave imager prelaunch hot load calibration," *IEEE Trans. Geosci. Remote Sens.*, vol. 41, no. 9, pp. 4731–4742, Sep. 2013.

[5] S. T. Brown, S. Desai, S. Keihm, and C. Ruf, "JMR noise diode stability and recalibration methodology after three years on-orbit," in *Proc. MicroRad*, San Juan, Puerto Rico, 2006, pp. 7–12.
[6] S. T. Brown, S. Desai, W. Lu, and A. B. Tanner, "On the long-tern stability of microwave radiometers using noise diodes for calibration," *IEEE Trans. Geosci. Remote Sens.*, vol. 45, no. 7, pp. 1908–1920, May 2007.
[7] T. Meissner and F. J. Wentz, "GMI calibration algorithm and analysis theoretical basis document," *Remote Sens. Syst.*, Santa Rosa, CA, USA, Rep. 051707, 2012.
[8] T. Mo, M. D. Goldberg, D. S. Crosby, and Z. Cheng, "Recalibration of the NOAA microwave sounding unit," *J. Geophys. Res.*, vol. 106, no. D10, pp. 10,145–10,150, 2001. doi:10.1029/2001JD900027.
[9] D. Draper, "Calibration data book for global precipitation measurement (GPM) microwave imager," *Ball Aerosp. Technol. Corp.*, Boulder, CO, USA, Rep. 2344649, 2014. Available: ftp://trmmopen.gsfc.nasa.gov
[10] D. M. Levine *et al.*, "Aquarius radiometer status," in *Proc. MicroRad*, Pasedena, CA, USA, 2014, pp. 226–227.
[11] Wikipedia. (2014). *DirecTV-10* [Online]. Available: http://en.wikipedia.org/wiki/DirecTV-10. Accessed on: Dec. 5, 2014.
[12] National Telecommunications & Information Administration. (2014). *United States Frequency Allocation Chart* [Online] 2014, http://www.ntia.doc.gov/page/2011/united-states-frequency-allocation-chart. Accessed on: Dec. 5, 2014.

David W. Draper (M'12) received the B.S. and Ph.D. degrees in electrical engineering from Brigham Young University, Provo UT, USA, in 2000 and 2003, respectively.

From 2004 until the present, he has been with Ball Aerospace & Technologies Corp. Boulder, CO, USA, as a Systems Engineer on the OMPS and GMI programs. His research interests and experience from industry and academia include estimation theory, active and passive microwave remote sensing, microwave radiometer calibration techniques, and radiometer RFI mitigation.

Dr. Draper is a member of Tau Beta Pi, and was a Fellow of that society in 2000–2001. He received the IEEE Geoscience and Remote Sensing Society Transaction Prize Paper Award in 2004.

David A. Newell received the B.S. and M.S. degrees in aerospace engineering from the University of Colorado, Boulder, CO, USA.

He worked with the Jet Propulsion Laboratory, Pasadena, CA, USA, from 1991 to 1995 where he was the Systems Engineer for the SeaWinds Scatterometer. He has worked with Ball Aerospace from 1995 to the present. He is currently the Chief Systems Engineer on the GMI instrument. He has authored a number of papers on microwave instrument design and calibration.

Darren S. McKague (M'08) received the Ph.D. degree in astrophysical, planetary, and atmospheric sciences from the University of Colorado, Boulder, CO, USA, in 2001.

He is the Assistant Director of the Space Physics Research Laboratory and an Assistant Research Scientist with the Department of Atmospheric, Oceanic, and Space Sciences with the University of Michigan, Ann Arbor, MI, USA. Prior to working for Michigan, he worked as a Systems Engineer with Ball Aerospace and with Raytheon, and as a Research Scientist with Colorado State University, Fort Collins, CO, USA. His research interests include remote sensing with emphases on the development of space-borne microwave remote sensing hardware, passive microwave calibration techniques, and mathematical inversion techniques for geophysical retrievals. His experience with remote sensing hardware includes systems engineering for several advanced passive and active instrument concepts and the design of the calibration subsystem on the Global Precipitation Mission (GPM) Microwave Imager (GMI) as well as the development of calibration and inter-calibration techniques for the GPM constellation. His algorithm experience includes the development of a near-real time algorithm for the joint retrieval of water vapor profiles, temperature profiles, cloud liquid water path, and surface emissivity for the Advanced Microwave Sounding Unit (AMSU), Colorado State University, and the development of the precipitation rate, precipitation type, sea ice, and sea surface wind direction algorithms for the risk reduction phase of the Conical scanning Microwave Imager/Sounder (CMIS).

Jeffrey R. Piepmeier (S'93–M'99–SM'10) earned the B.S. degree in engineering (electrical concentration) from LeTourneau University, Longview, TX, USA, in 1993, and the M.S. and Ph.D. degrees in electrical engineering from Georgia Institute of Technology, Atlanta, GA, USA, in 1994 and 1999, respectively.

He is currently an Associate Head with the Microwave Instruments and Technology Branch, NASA's Goddard Space Flight Center, Aquarius Science Team Member, and Instrument Scientist for the SMAP radiometer and GPM Microwave Imager (GMI). Previously, he worked with Vertex Communications Corporation and was a Schakleford Fellow with the Georgia Tech Research Institute. His research interests include microwave radiometry and technology development to enable the next generation of microwave sensors.

Dr. Piepmeier is a member of URSI (Commission F) and the American Geophysical Union. He is a past Chairperson of the GRSS Instrumentation and Future Technologies Technical Subcommittee and past Chairperson of the National Academies' Committee on Radio Frequencies (CORF). He was the recipient of an Excellence in Federal Career Gold Award (Rookie-of-the-year) in 2000 and was a 2002 NASA Earth Science New Investigator. He has received four NASA Group Achievement Awards and the NASA Exceptional Engineering Achievement Medal for advances in RFI mitigation technology and the NASA Exception Achievement Medal for significant contributions to the Aquarius/SAC-D mission.